

Hollow Beam Optical Ponderomotive Trap for Ultracold Neutral Plasma

S. A. Saakyan 

Joint Institute for High Temperatures, Russian Academy of Sciences, Moscow 125412, Russia*

(Dated: December 16, 2025)

Rapidly oscillating, inhomogeneous electromagnetic field from laser exert a force that repels charged particles from regions of high light intensity. We propose and analyze a flat-bottomed hollow-beam ponderomotive optical trap for an ultracold neutral plasma (UNP), driven by a high-power CO₂ laser. Molecular dynamics simulations show that the plasma and Rydberg atoms are effectively trapped within a nearly uniform dark region bounded by repulsive light walls. In contrast to RF traps, flat-bottomed traps yield a small density-weighted mean ponderomotive energy per electron, while the UNP collision frequency is far below the laser frequency, thereby making collisional absorption negligible and does not limit the lifetime of the trap. This approach could enhance antimatter production and storage.

Ponderomotive confinement is the opposite effect of the well-known ponderomotive acceleration of charged particles [1–3]. The ponderomotive force is proportional to the gradient of the cycle-averaged field intensity and repels charged particles from regions of high field amplitude [4, 5]. Ponderomotive traps (PTs) are widely used to confine non-neutral, single-component plasmas, such as ions or dusty particles in RF traps [6–9], as well as electrons in ponderomotive optical potentials [5, 10–12], and Rydberg atoms in bottle-beam traps [13, 14] or ponderomotive lattices [15, 16]. By contrast, confinement of quasi-neutral plasmas in PTs is limited by collisional absorption (inverse bremsstrahlung), which rapidly heats the electrons in an external oscillating field [17–19]. These limitations can be bypassed using optical box or hollow-beam traps. Recent advances in light shaping have enabled the creation of sculpted optical potentials for neutral-atom confinement [20]. Blue-detuned optical boxes use optical-dipole forces to confine atoms in dark, flat-bottom regions, suppressing photon scattering and ac-Stark shifts and yielding uniform-density samples. Applying a flat-bottom hollow-beam trap to an ultracold neutral plasma (UNP) [21–24] minimizes the density-weighted mean ponderomotive energy per electron by analogy with neutral-atom dark boxes, where scattering is suppressed. Additionally, because the optical drive frequency is much larger than the electron–ion collision rate in UNPs, collisional absorption is negligible on trapping timescales [25, 26].

In this Letter, we propose and analyze a novel UNP confinement method using the dark core of a hollow laser beam via molecular dynamics (MD) simulations. Simulations show that a two-component lithium plasma and Rydberg atoms are confined within a nearly uniform dark core bounded by repulsive light walls. We identify optimal experimental parameters and show that the trap simultaneously stores high-density UNP clusters and Rydberg states formed by three-body recombination, enabling dual trapping of UNP and Rydberg atoms. These capabilities suggest potential applications for trapping antiproton-positron plasmas and producing high-density

positronium samples [27–29].

The ponderomotive force $\mathbf{F}_p = -\nabla U_p$ acts on a free charged particle in a rapidly oscillating, inhomogeneous electromagnetic field, where $U_p = e^2(2m_{e,i}\omega^2c\varepsilon_0)^{-1}I(r)$ is the ponderomotive energy of the particle [30]. Here, e is the elementary charge, $m_{e,i}$ is the mass of the electron or ion, ω is the angular frequency of the optical field, and $I(r)$ is the optical field intensity distribution.

LG_{0ℓ} is an example of a laser beam with a minimum on the axis [31]. The intensity distribution of the hollow beam at the waist is given by

$$I(r) = P_0 \frac{2^{\ell+1} r^{2\ell}}{\pi \ell! w_{0\ell}^{2(\ell+1)}} \exp\left[-\frac{2r^2}{w_{0\ell}^2}\right], \quad (1)$$

where P_0 is the laser power and $w_{0\ell}$ is the beam waist. We use the single-ringed LG_{0ℓ} beam, with a radial mode index $p = 0$ and a dark spot at the optical axis, where ℓ is the azimuthal index [32]. In this configuration, the plasma trapped in the dark core of the LG_{0ℓ} beam lacks a restoring force along the beam axis. This force can be introduced by adding plugging beams to the LG_{0ℓ} setup [31]. Alternatively, intersecting multiple LG_{0ℓ} beams can create a near-spherical (bicylinder) trapping volume, or a three-dimensional single-beam configuration can be used as described in [11, 12]. For simplicity, we use a spherically symmetric LG potential, so in (1), the distance is $r = \sqrt{x^2 + y^2 + z^2}$.

Figure 1(a) shows the cross-sections of the ponderomotive potential U_p normalized to its peak value U_{p0} . The maximum intensity of the LG_{0ℓ} beam occurs at $r_0 = w_{0\ell}(\ell/2)^{1/2}$. The peak potential U_{p0} corresponds to the peak intensity $I(r_0)$. We vary $w_{0\ell} = \{124, 88, 62, 31\} \mu\text{m}$ for different $\ell = \{1, 2, 4, 16\}$ to keep the peak separation constant at $r_0 = 88 \mu\text{m}$. The peak intensities are many orders of magnitude below relativistic levels [33], and we do not consider the orbital angular momentum of the LG beams [34]. We assume that the particles are randomly distributed inside the trap volume with a Gaussian density distribution $n(\mathbf{r}) = n_0 \exp[-r^2/(2\sigma_0^2)]$, where the initial size is $\sigma_0 = 30 \mu\text{m}$. The dashed line in Fig. 1(a) represents the density profile of the UNP, normalized to

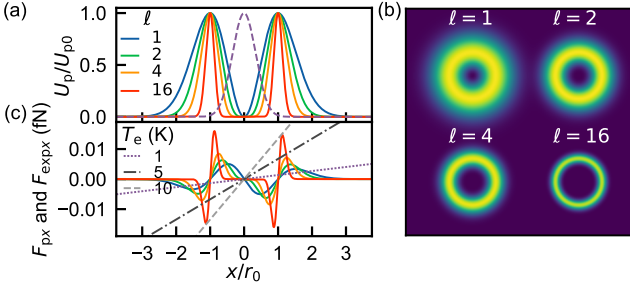


FIG. 1. Optical ponderomotive potential shape and properties. (a) Cross-sections of the ponderomotive potential for electrons normalized to its peak value U_{p0} for various azimuthal indices ℓ . The dashed curve shows the initial UNP density distribution with $\sigma_0 = 30 \mu\text{m}$ along one axis. (b) Intensity profiles of the $\text{LG}_{0\ell}$ trap for selected ℓ values. (c) Ponderomotive force on electrons and the force from electron thermal pressure. Solid curves represent F_{px} for $\ell = \{16, 4, 2, 1\}$ with fixed potential depth $U_{p0}/k_B = 20 \text{ K}$; dashed curves show F_{expx} for $T_e = \{1, 5, 10\} \text{ K}$.

the peak density $n_0 = N_{0i,e}/(2\sqrt{2}\pi^{3/2}\sigma^3)$. Higher ℓ values enhance the force and enlarge the dark region at the trap center, making these configurations suitable for optical boxes due to their low scattering rate [20]. Figure 1(b) shows the intensity profile of the $\text{LG}_{0\ell}$ beam at the waist.

After initial thermal equilibration, UNP expansion is well described by hydrodynamic treatment [21]. We estimate the per-ion force driving the ion expansion and compare it with the ponderomotive force acting primarily on electrons. The electron thermal pressure creates a per-ion force $\mathbf{F}_{\text{exp}}(\mathbf{r}) = -k_B T_e \nabla n(\mathbf{r})/n(\mathbf{r})$ [21, 23]. For simplicity, we neglect variations in electron temperature during UNP expansion [23, 35]. Figure 1(c) shows the ponderomotive force component acting on the electrons inside the trap, with $U_{p0}/k_B = 20 \text{ K}$, compared to the electron thermal pressure force. According to these simple estimates, the PT significantly affects plasma expansion when $k_B T_e/U_{p0} < 1$ [36]. However, plasma dynamics is more complex than this simple hydrodynamic model suggests.

The ideas presented so far have been tested numerically with the MD simulation method. Standard kinetic theories failed to describe the strongly coupled plasma properties [21]. One of the most effective ways to gain insight into UNP is through numerical modelling of non-equilibrium UNP using the MD method. We model the electron-electron and ion-ion interactions with a pure Coulomb potential. For electron-ion interactions, the Coulomb potential with repulsive core is used [37]. Two-component plasma simulations were conducted in open-boundary conditions using open-source code LAMMPS [38]. The repulsion length scale is fixed at the value $\alpha = a_{\text{ws}}/80 \approx 60 \text{ nm}$ for all simulations. This length was chosen to be small enough to have no influence on the simulation results, as we verified by varying the

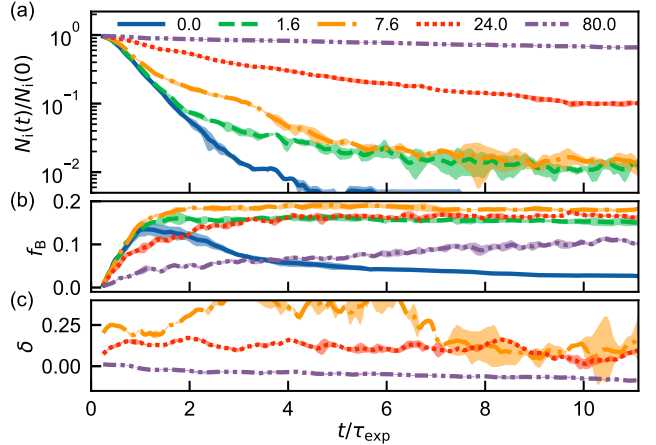


FIG. 2. Time evolution of the normalized number of ions (a), the fraction of bound states (b) and the charge imbalance (c) inside the PT ($r < r_0$) for different trap depths U_{p0}/k_B (indicated in the legend in K). The initial number of particles $N_{i,e}(0) = 500$, corresponds to an initial peak density $n_0 = 1.18 \times 10^9 \text{ cm}^{-3}$, $\ell = 16$ and $T_e(0) = 1 \text{ K}$. Curves for $U_{p0}/k_B = 0$ and 1.6 K in panel (c) are excluded for clarity due to high uncertainties.

repulsion length scale value between 30 and 100 nm. The integration time step is $\delta t = 0.2 \text{ ps}$, which ensures that total energy is conserved to better than 1%. We vary the initial number of ions and electrons $N_i = N_e = 100 \dots 500$ in constant size $\sigma_0 = 30 \mu\text{m}$ UNP to change the initial density in the PT. The Debye screening length for all densities is $\lambda_D \ll \sigma_0$. For the numerical simulations, we choose light lithium ions. Lithium is the closest element to hydrogen and is widely used for different laser cooling experiments with Rydberg atoms [39], photoionization phenomena study [40, 41], ion beam microscopy [42], and quantum degenerate gases [20].

The number of ions inside the PT ($r < r_0$) vs time after photoionization is presented in Fig. 2(a) for different values of U_{p0} and $N_i = N_e = 500$ corresponding to the initial peak density $n_0 = 1.18 \times 10^9 \text{ cm}^{-3}$. According to the hydrodynamical description, the expansion time for light lithium ions is $\tau_{\text{exp}} = (m_i \sigma_0^2 / [k_B T_e(0)])^{1/2} \approx 0.9 \mu\text{s}$ for initial plasma size $\sigma_0 = 30 \mu\text{m}$ and $T_e = 1 \text{ K}$. We investigate plasma properties inside the PT volume $r < r_0$. The expansion time without PT from this volume [the lowest curve in Fig. 2(a)] is $\tau_{r_0} = 0.83 \mu\text{s}$.

By analyzing the MD data, we identify the classical bound states according to [43]. The electron is considered bound to the ion if the following criteria are met simultaneously: its energy drops significantly below the energy of the free electron; the rotation angle around the ion, integrated for a selected time interval $10^6 \delta t$, is more than some critical angle. After manually analyzing the trajectories, we introduced the final criterion that the electron-ion distance remain below 50α over the same time interval and set the critical rotation angle to 8π .

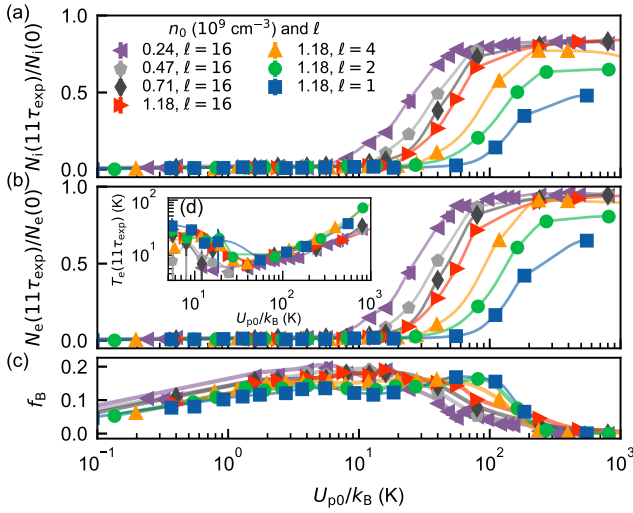


FIG. 3. The normalized numbers of ions (a), electrons (b), and bound states (c) inside the trap volume, as well as the electron temperature (d), vs the trap depth U_{p0}/k_B after $t = 11\tau_{\text{exp}}$, for different initial UNP densities n_0 and various trap shapes ℓ .

The time evolution of the fraction of bound states inside the trap volume is presented in Fig. 2(b). The number of bound particles inside the trap ($r < r_0$) is normalized to the initial particle number $N_{i,e}(0)$. We identify bound particles and separate their contribution to all plasma parameters [37]. Without PT, a sufficient number of electrons escape from the plasma after ionization. The charge imbalance described as $\delta = (N_i - N_e)/N_i$ decreases with PT peak depth [see Fig 2(c)], along with an increase in the number of trapped electrons and ions. A shaded region in the figure represents the calculation uncertainties extracted as the standard deviation of the few independent simulations with different initial random configurations and different random velocity distributions resulting in $T_e = 1$ K and $T_i = 1$ mK. The bound state fraction f_B is the same for the $\alpha = 30$ nm and 100 nm. There is no difference found within the uncertainties.

The trapping efficiency depends mainly on the UNP temperature. The overall trapping efficiency depends on the temperature settled in the UNP after the equilibration of electrons and ions due to the DIH [21, 35, 44, 45]. This settled temperature strongly depends on the initial density of the UNP. In Fig. 3, N_i , N_e , and f_B at the time step $t = 11\tau_{\text{exp}}$ are shown for plasmas with different initial peak densities and different PT configurations ℓ . Obviously, the trapping efficiency increases with the trap depth, especially for electrons (the charge imbalance δ in Fig. 2(c) becomes negative, i.e. the number of electrons is higher than that of ions). When the UNP temperature becomes comparable to the trap depth, the plasma starts to confine inside the PT. In Fig. 3(d), the kinetic temperature of electrons depending on the peak trap depth is shown. At higher U_{p0} , the formation of the bound-state

fraction is suppressed [see Fig. 3(c)] due to the increase in the electron kinetic temperature and the oscillation frequency of the electrons inside the potential wells. Even for low trap depth $U_{p0}/k_B \ll 10$ K, the bound states formed in the UNP are successfully confined inside the PT volume.

For a single electron in a PT with $\ell = 1$, if the oscillation amplitude is small, the ponderomotive potential is approximately parabolic, and the oscillation frequency is $\omega_e = [2P_0/(cm_e^2\pi w_{01}^4\varepsilon_0\omega^2)]^{1/2}$ [10]. Numerical simulations for $\ell = 1$ with small amplitudes are in excellent agreement with this calculated frequency ω_e .

The coupling strength of the UNP is quantified by the coupling parameter $\Gamma_{e,i} = e^2/(4\pi\varepsilon_0 a_{\text{WS}} k_B T_{e,i})$, which represents the ratio of the Coulomb potential energy at the average interparticle spacing a_{WS} to the average kinetic energy. For a UNP confined in the PT, the ion coupling parameter lies in the range $\Gamma_i \approx 1\text{--}3$, while the electrons remain weakly coupled with $\Gamma_e \approx 0.1\text{--}0.3$ (values vary with trap depth). These coupling parameters are comparable to those reported in typical UNP experiments [21].

Figure 4(a) shows the time evolution of the peak electron density n_e for several trap depths U_{p0}/k_B , at fixed $\ell = 16$. The plasma confined in the trap follows the inner shape of the PT. For higher ℓ , the plasma forms a homogeneous density profile with exponential decay, similar to neutral gases in optical boxes [20] or UNP from magnetic traps [46]. Initially Gaussian-distributed particles in the PT evolve into a flat-top distribution $n_{e,i}(\mathbf{r}) = n_{0e,i} \exp[-(1/2)([x^2 + y^2 + z^2]/\sigma^2)^k]$ with $k > 1$. At $t = 11\tau_{\text{exp}}$ for $U_{p0}/k_B = 56$ K, the radial distribution is well described by a flat-top function with $k = 6$ [see Fig. 4(b)]. Following creation in the PT, the expanding plasma encounters the potential walls and rapidly equilibrates ($t < 5\tau_{\text{exp}}$), exhibiting damped oscillations in the peak density and size σ [Fig. 4(a)]. We also observe that lower ℓ values correspond to higher amplitude oscillations with well-defined frequencies.

Figure 4(c) shows the plasma lifetime τ in the PT as a function of trap depth U_{p0}/k_B for two initial densities. The lifetime is obtained by fitting the post-equilibration decay of the ion and electron numbers $N_{i,e}(t)$, as illustrated in Fig. 2(a). Ion confinement by the PT is weak. Ions are held primarily by the electron space-charge potential within the trap. Accordingly, increasing the trapped population extends the ion lifetime, which at sufficiently large populations may approach the electron lifetime. Three-body recombination (TBR) heats the plasma by creating bound states and limits the lifetime in the PT. This heating channel is included in our computational model.

In the simulations the PT acts through the cycle-averaged ponderomotive force, and the electron quiver motion in the optical field is neglected. Conventional radio-frequency PTs for non-neutral particles do not con-

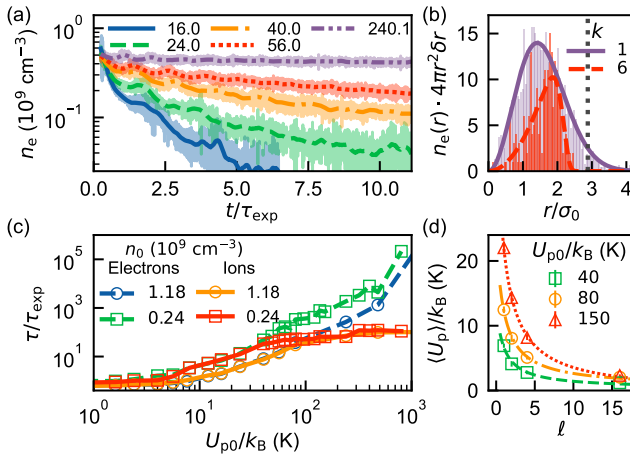


FIG. 4. (a) Peak density $n_e(t)$ for several trap depths U_{p0}/k_B (in K, see legend). (b) Radial density profiles at $t = 0$ and $t \approx 11\tau_{\text{exp}}$ for $U_{p0}/k_B = 56$ K. During equilibration the initially Gaussian profile ($k = 1$) evolves toward a flat-top shape ($k = 6$) with damped oscillations; the dotted vertical line corresponds to r_0 value. (c) The lifetime τ of electrons (dashed line) and ions (solid line) inside the PT versus U_{p0}/k_B for two different initial densities. For panels (a)–(c) $\ell = 16$ azimuthal index is used. (d) Density-weighted mean ponderomotive energy per electron $\langle U_{p0} \rangle/k_B$ vs ℓ , points are simulation results and solid lines are least-squares fits to $A/(\ell+1) + c$, consistent with the thin-shell model expectation $\langle U_p \rangle \propto U_{p0}/(\ell + 1)$.

fine a neutral plasma because collisional absorption, or inverse bremsstrahlung (IB), causes rapid electron heating. UNPs in external RF and microwave fields have been used to study collisional heating [19, 47, 48]. The IB heating rate depends on the ratio of the electron–ion collision frequency $\nu_{e,i}$ to the drive frequency [26]. In typical UNP conditions [21–24] one finds $\nu_{e,i}$ far below the GHz range. As a result, even intense laser fields produce negligible IB heating. Energy acquired by an electron in one half-cycle is returned in the next unless a collision interrupts the motion, and the low collision probability makes the net per-cycle heating negligible.

In conventional transport theory, the power absorbed per electron is $P_{ei} \approx 2\langle U_p \rangle \nu_{ei}$ [49], where the density-weighted mean per-electron ponderomotive energy, $\langle U_p \rangle = \int U_p(r) n_e(r) d^3r / \int n_e(r) d^3r$, is determined numerically from the MD data and is shown in Fig. 4(d) for several ℓ values and for $U_{p0}/k_B = 40, 80$, and 150 K. The trajectory-averaged potential matches the ensemble average, consistent with an ergodic electron subsystem in a stationary two-temperature plasma. In a flat-bottomed trap only electrons near the walls sample the optical intensity. This thin-shell sampling yields the scaling $\langle U_p \rangle \propto U_{p0}/(\ell + 1)$, consistent with our MD results. For $\langle U_p \rangle = 2.5$ K this gives $P_{ei}/k_B \approx 200$ K/ μ s. More bremsstrahlung-specific models for the optical regime predict strong high-frequency suppression of absorption, so the transport estimate overstates heating in our con-

ditions [25, 26].

We also perform full-field simulations of the PT with an oscillating electric field corresponding to $U_{p0} = 96$ K at density 0.24×10^9 cm $^{-3}$ after equilibration. No measurable heating is observed over 150 ns, and the trapping efficiency matches the cycle-averaged calculations. To map the frequency dependence, we simulate a uniform UNP with periodic boundaries in uniform external fields from 50 GHz to 30 THz, which includes the CO₂ laser frequency [25, 26]. For RF range external fields, the IB heating agrees with theoretical estimates. At optical frequencies near a CO₂ laser we find no measurable IB heating over the simulated timescales. These calculations indicate that optical-frequency heating of low-density UNPs is negligible [50].

The novel PT holds significant potential for various applications. It enables dual trapping of charged particles and Rydberg atoms in the dark region and can guide UNP or antimatter plasmas, assisting collimation in modern ion and electron microscopy [51]. Ground-state particles can also be confined at intensity maxima by dipole forces, but a far-off-resonant CO₂ optical dipole trap provides only a shallow potential [52]. For antihydrogen, photon scattering is negligible while recombination produces atoms hotter than the trap depth, so their subsequent capture is inefficient [27].

Several technical challenges exist for the experimental realization of the PT. Modern CO₂ lasers typically provide cw output power around 20 kW, while conventional cold-atoms experiments use IR lasers with two orders of magnitude less power. One solution is to use an optical cavity to achieve the required average power level [53–55]. Tight focusing limits trap volume and the trapped-electron number, shortening ion lifetimes, so elongated cylindrical geometries are preferable for larger, lower-density samples. Bound states are efficiently confined even at low depths [Figs. 2(b), 3(c)], enabling guided extraction of the bound fraction from antimatter plasmas, similar to traveling-lattice antihydrogen beams [56]. Hybrid schemes that combine PT with magnetic confinement could suppress electron losses along field lines with reduced optical power [23] and may enable access to strongly coupled, liquid- or crystal-like UNP regimes [6].

In this work, we have proposed and analyzed a hollow-beam ponderomotive trap for ultracold neutral plasmas and demonstrated, via simulations, confinement of a two-component lithium plasma and Rydberg atoms within a dark, flat-bottom region. The combination of thin-shell sampling and optical drive frequencies suppresses inverse bremsstrahlung absorption. Full-field simulations confirm the absence of measurable heating at the CO₂ frequency and validate the cycle-averaged description. Ion lifetimes increase with trapped population and approach electron lifetimes at large populations. These results establish a practical parameter window for the flat-bottom optical confinement of UNPs and outline routes to im-

prove performance using cavity enhancement, high-order LG modes, elongated geometries, and hybrid optical-magnetic trapping. This approach enables simultaneous trapping of free charges and their Rydberg products, potentially advancing antimatter plasma trapping and production.

The supporting data for this Letter including MD trajectories and necessary LAMMPS input are openly available in the data repository [50].

The author wishes to thank A.A. Bobrov, B.V. Zelenov, B.B. Zelenov, V.A. Sautenkov, E.V. Vikhrov and S. Ya. Bronin for very useful discussions. This work was supported by the Russian Science Foundation, Grant No. 23-72-10031 and by the Ministry of Science and Higher Education of the Russian Federation (State Assignment No. 075-00270-24-00) with respect to providing the computational resources.

* saakyan@ihed.ras.ru

- [1] G. V. Stupakov and M. Zolotorev, Ponderomotive laser acceleration and focusing in vacuum for generation of attosecond electron bunches, *Phys. Rev. Lett.* **86**, 5274 (2001).
- [2] F. He, W. Yu, P. Lu, H. Xu, L. Qian, B. Shen, X. Yuan, R. Li, and Z. Xu, Ponderomotive acceleration of electrons by a tightly focused intense laser beam, *Phys. Rev. E* **68**, 046407 (2003).
- [3] E. Esarey, C. B. Schroeder, and W. P. Leemans, Physics of laser-driven plasma-based electron accelerators, *Rev. Mod. Phys.* **81**, 1229 (2009).
- [4] A. Gaponov and M. Miller, Potential wells for charged particles in a high-frequency electromagnetic field, *J. Exp. Theor. Phys.* **34**, 242 (1958).
- [5] N. Phillips and J. Sanderson, Trapping of electrons in a spatially inhomogeneous laser beam, *Phys. Lett.* **21**, 533 (1966).
- [6] D. H. E. Dubin and T. M. O'Neil, Trapped nonneutral plasmas, liquids, and crystals (the thermal equilibrium states), *Rev. Mod. Phys.* **71**, 87 (1999).
- [7] V. E. Fortov, A. G. Khrapak, S. A. Khrapak, V. I. Molotkov, and O. F. Petrov, Dusty plasmas, *Phys.-Usp.* **47**, 447 (2004).
- [8] D. Leibfried, R. Blatt, C. Monroe, and D. Wineland, Quantum dynamics of single trapped ions, *Rev. Mod. Phys.* **75**, 281 (2003).
- [9] C. Matthiesen, Q. Yu, J. Guo, A. M. Alonso, and H. Häffner, Trapping electrons in a room-temperature microwave Paul Trap, *Phys. Rev. X* **11**, 011019 (2021).
- [10] C. Moore, Confinement of electrons to the centre of a laser focus via the ponderomotive potential, *J. Mod. Opt.* **39**, 2171 (1992).
- [11] J. L. Chaloupka, Y. Fisher, T. J. Kessler, and D. D. Meyerhofer, Single-beam, ponderomotive-optical trap for free electrons and neutral atoms, *Opt. Lett.* **22**, 1021 (1997).
- [12] J. L. Chaloupka and D. Meyerhofer, Observation of electron trapping in an intense laser beam, *Phys. Rev. Lett.* **83**, 4538 (1999).
- [13] D. Barredo, V. Lienhard, P. Scholl, S. de Leseleuc, T. Boulier, A. Browaeys, and T. Lahaye, Three-dimensional trapping of individual Rydberg atoms in ponderomotive bottle beam traps, *Phys. Rev. Lett.* **124**, 023201 (2020).
- [14] B. Ravon, P. Méhaignerie, Y. Machu, A. D. Hernández, M. Favier, J. M. Raimond, M. Brune, and C. Sayrin, Array of individual circular Rydberg atoms trapped in optical tweezers, *Phys. Rev. Lett.* **131**, 093401 (2023).
- [15] S. Dutta, J. Guest, D. Feldbaum, A. Walz-Flannigan, and G. Raithel, Ponderomotive optical lattice for Rydberg atoms, *Phys. Rev. Lett.* **85**, 5551 (2000).
- [16] S. E. Anderson, K. C. Younge, and G. Raithel, Trapping Rydberg atoms in an optical lattice, *Phys. Rev. Lett.* **107**, 263001 (2011).
- [17] V. P. Silin, Nonlinear high-frequency plasma conductivity, *Sov. Phys. JETP* **20** (1965).
- [18] P. Mulser and D. Bauer, *High power laser-matter interaction*, Vol. 238 (Springer Science & Business Media, 2010).
- [19] P. W. Smorenburg, L. P. J. Kamp, and O. J. Luiten, Heating mechanisms in radio-frequency-driven ultracold plasmas, *Phys. Rev. A* **85**, 063413 (2012).
- [20] N. Navon, R. P. Smith, and Z. Hadzibabic, Quantum gases in optical boxes, *Nat. Phys.* **17**, 1334 (2021).
- [21] T. C. Killian, T. Pattard, T. Pohl, and J. Rost, Ultracold neutral plasmas, *Phys. Rep.* **449**, 77 (2007).
- [22] T. K. Langin, G. M. Gorman, and T. C. Killian, Laser cooling of ions in a neutral plasma, *Science* **363**, 61 (2019).
- [23] G. M. Gorman, M. Warrens, S. Bradshaw, and T. Killian, Magnetic confinement of an ultracold neutral plasma, *Phys. Rev. Lett.* **126**, 085002 (2021).
- [24] B. Zelenov, E. Vilshanskaya, N. Morozov, S. Saakyan, A. Bobrov, V. Sautenkov, and B. Zelenov, Steady-state ultracold plasma created by continuous photoionization of laser cooled atoms, *Phys. Rev. Lett.* **132**, 115301 (2024).
- [25] D. Turnbull, J. Katz, M. Sherlock, A. L. Milder, M. S. Cho, L. Divol, N. R. Shaffer, D. J. Strozzi, P. Michel, and D. H. Froula, Reconciling calculations and measurements of inverse bremsstrahlung absorption, *Phys. Plasmas* **31**, 063304 (2024).
- [26] D. Turnbull, J. Katz, M. Sherlock, L. Divol, N. R. Shaffer, D. J. Strozzi, A. Colaïtis, D. H. Edgell, R. K. Follett, K. R. McMillen, P. Michel, A. L. Milder, and D. H. Froula, Inverse bremsstrahlung absorption, *Phys. Rev. Lett.* **130**, 145103 (2023).
- [27] M. Ahmadi, B. Alves, C. Baker, W. Bertsche, A. Capra, C. Carruth, C. Cesar, M. Charlton, S. Cohen, R. Collister, *et al.*, Observation of the 1s–2p Lyman- α transition in antihydrogen, *Nature* **561**, 211 (2018).
- [28] E. Stenson, S. Nißl, U. Hergenhahn, J. Horn-Stanja, M. Singer, H. Saitoh, T. S. Pedersen, J. Danielson, M. Stoneking, M. Dickmann, *et al.*, Lossless positron injection into a magnetic dipole trap, *Phys. Rev. Lett.* **121**, 235005 (2018).
- [29] P. Steinbrunner, T. M. O'Neil, M. R. Stoneking, and D. H. E. Dubin, Thermal equilibrium of collisional non-neutral plasma in a magnetic dipole trap, *J. Plasma Phys.* **89**, 935890401 (2023).
- [30] S. Zhang, F. Robicheaux, and M. Saffman, Magic-wavelength optical traps for Rydberg atoms, *Phys. Rev. A* **84**, 043408 (2011).
- [31] T. Kuga, Y. Torii, N. Shiokawa, T. Hirano, Y. Shimizu, and H. Sasada, Novel optical trap of atoms with a dough-

nut beam, *Phys. Rev. Lett.* **78**, 4713 (1997).

[32] J. Zhang, S.-J. Huang, F.-Q. Zhu, W. Shao, and M.-S. Chen, Dimensional properties of Laguerre–Gaussian vortex beams, *Appl. Opt.* **56**, 3556 (2017).

[33] G. Malka and J. Miquel, Experimental confirmation of ponderomotive-force electrons produced by an ultrarelativistic laser pulse on a solid target, *Phys. Rev. Lett.* **77**, 75 (1996).

[34] A. Denoeud, L. Chopineau, A. Leblanc, and F. Quéré, Interaction of ultraintense laser vortices with plasma mirrors, *Phys. Rev. Lett.* **118**, 033902 (2017).

[35] M. Lyon and S. L. Rolston, Ultracold neutral plasmas, *Rep. Prog. Phys.* **80**, 017001 (2016).

[36] P. Smorenburg, L. Kamp, and O. Luiten, Ponderomotive manipulation of cold subwavelength plasmas, *Phys. Rev. E* **87**, 023101 (2013).

[37] S. K. Tiwari, N. R. Shaffer, and S. D. Baalrud, Thermodynamic state variables in quasiequilibrium ultracold neutral plasma, *Phys. Rev. E* **95**, 043204 (2017).

[38] A. P. Thompson, H. M. Aktulga, R. Berger, D. S. Bolintineanu, W. M. Brown, P. S. Crozier, P. J. in't Veld, A. Kohlmeyer, S. G. Moore, T. D. Nguyen, *et al.*, LAMMPS—a flexible simulation tool for particle-based materials modeling at the atomic, meso, and continuum scales, *Comput. Phys. Commun.* **271**, 108171 (2022).

[39] S. Wüster and J. M. Rost, Rydberg aggregates, *J. Phys. B* **51**, 032001 (2018).

[40] M. Schuricke, G. Zhu, J. Steinmann, K. Simeonidis, I. Ivanov, A. Kheifets, A. N. Grum-Grzhimailo, K. Bartschat, A. Dorn, and J. Ullrich, Strong-field ionization of Lithium, *Phys. Rev. A* **83**, 023413 (2011).

[41] S. Saakyan, L. D'yachkov, S. Klimov, V. Sautenkov, and B. B. Zelener, Photoionization cross section of first excited state of Lithium, *Spectrochim. Acta B* **195**, 106503 (2022).

[42] J. J. McClelland, A. V. Steele, B. Knuffman, K. A. Twedt, A. Schwarzkopf, and T. M. Wilson, Bright focused ion beam sources based on laser-cooled atoms, *Appl. Phys. Rev.* **3** (2016).

[43] G. Bannasch and T. Pohl, Rydberg-atom formation in strongly correlated ultracold plasmas, *Phys. Rev. A* **84**, 052710 (2011).

[44] M. S. Murillo, Using fermi statistics to create strongly coupled ion plasmas in atom traps, *Phys. Rev. Lett.* **87**, 115003 (2001).

[45] D. Murphy and B. M. Sparkes, Disorder-induced heating of ultracold neutral plasmas created from atoms in partially filled optical lattices, *Phys. Rev. E* **94**, 021201 (2016).

[46] M. K. Warrens, G. M. Gorman, S. J. Bradshaw, and T. C. Killian, Expansion of ultracold neutral plasmas with exponentially decaying density distributions, *Phys. Plasmas* **28**, 022110 (2021).

[47] M. A. W. van Ninhuijs, J. Beckers, and O. J. Luiten, Collisional microwave heating and wall interaction of an ultracold plasma in a resonant microwave cavity, *New J. Phys.* **24**, 063022 (2022).

[48] T. M. Wilson, W.-T. Chen, and J. L. Roberts, Density-dependent response of an ultracold plasma to few-cycle radio-frequency pulses, *Phys. Rev. A* **87**, 013410 (2013).

[49] M. A. W. van Ninhuijs, K. A. Daamen, J. G. H. Franssen, J. Conway, B. Platier, J. Beckers, and O. J. Luiten, Microwave cavity resonance spectroscopy of ultracold plasmas, *Phys. Rev. A* **100**, 061801 (2019).

[50] S. A. Saakyan, 10.5281/zenodo.17939823.

[51] T. C. H. De Raadt, J. G. H. Franssen, and O. J. Luiten, Subpicosecond Ultracold Electron Source, *Phys. Rev. Lett.* **130**, 205001 (2023).

[52] R. Grimm, M. Weidemüller, and Y. B. Ovchinnikov, Optical dipole traps for neutral atoms, *Adv. At. Mol. Opt. Phys.* **42**, 95 (2000).

[53] D. Ganapathy, W. Jia, M. Nakano, V. Xu, N. Aritomi, T. Cullen, N. Kijbunchoo, S. Dwyer, A. Mullavey, and L. McCuller *et al.*, Broadband quantum enhancement of the LIGO detectors with frequency-dependent squeezing, *Phys. Rev. X* **13**, 041021 (2023).

[54] X.-Y. Lu, R. Chiche, K. Dupraz, F. Johora, A. Martens, D. Nutarelli, Y. Peinaud, V. Soskov, A. Stocchi, and F. Zomer *et al.*, Stable 500 kW average power of infrared light in a finesse 35 000 enhancement cavity, *Appl. Phys. Lett.* **124**, 251105 (2024).

[55] L. Carbone, C. Bogan, P. Fulda, A. Freise, and B. Willke, Generation of high-purity higher-order Laguerre-Gauss beams at high laser power, *Phys. Rev. Lett.* **110**, 251101 (2013).

[56] N. Madsen and M. Charlton, On the formation of anti-hydrogen beams using travelling optical lattices, *New J. Phys.* **23**, 073003 (2021).